Turbulence-Kinetic-Energy Budget in the Urban-Like Boundary Layer Using Large-Eddy Simulation

Geng Tian, Boris Conan, Isabelle Calmet

Noname manuscript No.
(will be inserted by the editor)

Turbulence Kinetic Energy Budget in the Urban-like Boundary Layer using Large-Eddy Simulation

Geng Tian[1,2] · Boris Conan[1,2] · Isabelle Calmet[1,2]

Received: DD Month YEAR / Accepted: DD Month YEAR

Abstract This work aims to describe and understand the turbulent processes at play in the lower part of the urban boundary layer through performing a large-eddy simulation of the flow over an urban-like canopy. This canopy is composed of a staggered array of cubes with a packing density of 25%, while the simulation models neutral thermal conditions at a Reynolds number (based on both velocity at the top of the domain and the domain height) of $Re = 50,000$. A dynamic Smagorinsky model is implemented in order to allow for energy backscattering from sub-grid scales. A wall refinement of the grid allows resolving the viscous sublayer. Turbulent statistics up to the third order, as well as each term of the turbulence kinetic energy budget, are computed individually everywhere in the domain. Results are discussed in relation to experimental and numerical data from the literature in order to describe the turbulent energy transfers occurring in the roughness sublayer. The fine grid resolution close to surfaces serves to analyze in depth the three-dimensional distribution of turbulence production inside the urban canopy layer. This analysis in turn leads to discovering areas, never previously documented in an urban-like canopy, of highly positive and highly negative production close to the surface, away from the well-known high production area in the shear layer. Furthermore, evidence of a close link between high and low production areas near the surfaces and singular points in the mean flow is presented, thus laying the groundwork for a simple pre-diagnostic tool to detect TKE production areas near surfaces.

Keywords Large-eddy simulation · OpenFOAM · Turbulence kinetic energy budget · Turbulence production · Urban canopy layer · Wall-bounded flow

G. Tian · B. Conan · I. Calmet

1. Ecole Centrale de Nantes, LHEEA UMR CNRS 6598, Nantes, France
2. Institut de Recherche en Sciences et Techniques de la Ville (IRSTV), FR CNRS 2488, Nantes, France

E-mail: boris.conan@ec-nantes.fr

1 Introduction

In the context of rapid urbanization, an understanding and accurate modeling of turbulent flow in the urban boundary layer (UBL) is of great importance in evaluating the influence of urban design on air quality and urban climate. The roughness sublayer (RSL) is the lowest part of the UBL (Oke, 1997) and where high momentum, heat and mass exchanges between the urban canopy layer (UCL) and the atmosphere take place (Rotach, 1999). The RSL extends from the ground surface up to 2 to 5 times the average building height, depending on the geometric arrangement of the element (Raupach et al., 1991; Cheng et al., 2007). The presence of roughness elements gives rise to complex flows consisting of vortical structures and low-momentum regions (Coceal et al., 2007b). The UCL is the lowest part of the RSL, lying below the average building height, where the flow is directly influenced by ground obstacles.

Over the past few decades, a number of field experiments (Christen et al., 2009; Inagaki and Kanda, 2010; Roth et al., 2015; Perret et al., 2016) and wind tunnel experiments (Macdonald, 2000; Cheng and Castro, 2002; Kastner-Klein and Rotach, 2004; Castro et al., 2006; Blackman and Perret, 2016; Blackman et al., 2017; Herpin et al., 2018; Monnier et al., 2018) have been conducted to investigate the nature of turbulence over urban-like canopies. These studies have extended the understanding of turbulent flow characteristics by determining the mean flow and main turbulent processes occurring within the RSL as a function of obstacle density, arrangement and height. Unsteady urban-like canopy flows have also been studied by means of Computational Fluid Dynamics (CFD) simulations using Direct Numerical Simulation (DNS) (Coceal et al., 2006, 2007a,b; Leonardi and Castro, 2010) and Large-Eddy Simulation (LES) (Kanda et al., 2004; Xie and Castro, 2006; Bou-Zeid et al., 2009; Kono et al., 2010; Tomas et al., 2016). Numerical studies show good agreement on both mean flow and turbulence statistics compared to the wind tunnel results. Since LES explicitly resolves the large flow-scales and introduces a subgrid-scale (SGS) model to parameterize the small-scale processes, it is considered as a powerful tool for simulating 3D unsteady flow more effectively than DNS when dealing with high Reynolds number flows. Numerical studies have made it possible to investigate non-neutral conditions and yielded a spatial description of the mean flow and standard turbulent characteristics (Tomas et al., 2016; Coceal et al., 2007a). More recently, several combined experimental/numerical studies have also been performed on cuboidal arrays (Tomas et al., 2017; Castro et al., 2017).

The turbulent mechanisms responsible for energy transfers both within and above the RSL can be investigated using the turbulence kinetic energy (TKE) budget. This method, based on an analysis of TKE sources and sinks in a fully-developed turbulent flow, serves to analyze TKE transfers. Over a flat and homogeneous surface, TKE production, an unsteady phenomenon by its very nature, is partially driven by hairpin-like turbulent structures near the ground (Adrian, 2007). The TKE budget terms only vary in the direction perpendicular to the surface and, far enough from the surface, a balance between

production and dissipation is observed (Kim et al., 1987; Lyons et al., 1989; Brooke and Hanratty, 1993). This property characterizes the energy transfer between scales in the inertial subrange and is the basis for several turbulence models and wall boundary conditions (Hudson et al., 1996).

The presence of obstacles inside an urban canopy layer is expected to destroy the homogeneity of the time-averaged TKE budget terms of a flat plate. Indeed, over a single wall-mounted cube, Yakhot et al. (2006) observed the distribution of production and enlighten negative production areas close to the foot of a cube and on its front face. They describe negative production regions by discussing the sign and magnitude of each production term. They suggest that "the flow dynamics in front of a cube is strongly affected by the negative energy production" and underline their proximity with stagnation lines.

In their experimental work on an urban-like arrangement of cubes, Castro et al. (2006) computed vertical profiles of the TKE budget at several locations upstream and downstream of a cube featuring a staggered arrangement. TKE dissipation was estimated from power spectral density measurements, and the pressure transport of TKE was deduced as the residual term needed to balance the TKE budget. These authors showed that TKE production is highest after the cube, where the shear stress (and vertical gradient of the velocity) is significant. They also observed that production is nearly balanced by dissipation above the RSL (greater than 4 times the obstacle height) and moreover that turbulent transport is an energy sink within the shear layer, i.e. just above the canopy. Blackman et al. (2017) investigated the TKE budget using Particle Image Velocimetry (PIV) over a 2D plane. In this work, the dissipation rate was evaluated using a Large-Eddy PIV (LE-PIV) model, based on use of a SGS model according to the methodology applied in LES. Despite some interesting findings, experimental restrictions tended to prevent capturing the three-dimensional flow field that often limits analysis of the TKE budget to one or two spatial dimensions, requiring researchers reconstitute the missing information (spatial gradients, dissipation) based on theoretical simplifications or modeling (Castro et al., 2006; Blackman et al., 2017). In addition, experimental constraints often prevent measuring turbulence very close to the wall. As opposed to plant canopy flows (Dwyer et al., 1997; Finnigan, 2000; Yue et al., 2008), very few numerical studies have analyzed in detail all TKE budget terms in an urban-like canopy. Giometto et al. (2016) computed the TKE budget over a realistic urban model and found that pressure transport is significant in the near-wall regions, while turbulent transport transfers the TKE produced above the canopy downwards into the urban canopy. Tomas et al. (2016) explicitly computed all TKE budget terms in order to study the effect of thermal stratification on the various terms, with an emphasis on the upper part of the RSL and the inertial layer.

As reported in the aforementioned literature, the TKE budget is very different around the obstacles of an urban-like boundary layer flow, as compared to a flat plate boundary layer flow. However, existing studies are mostly focused on the upper part of the RSL and leave open questions regarding TKE processes inside the urban canopy layer, namely:

- What is the relative contribution of the TKE budget terms at different locations inside an idealized UCL?
- How is TKE production spatially distributed in the UCL to maintain the boundary layer? To what extent does it differ from that of a flat plate or a single wall-mounted cube?
- Can TKE production within the urban canopy layer be correlated with mean flow distinctive features?

This article proposes tackling these questions by setting up and running a fine-scale LES over an urban-like canopy in order to directly compute each term of the TKE budget inside and outside the UCL without the need for any theoretical assumptions or further modeling beyond those of an LES. Results reveal areas never before documented of strong positive and negative turbulence production inside the UCL, in addition to improving the understanding of the main turbulent mechanisms in the RSL.

This study focuses on the fully-developed neutral turbulent flow over an array of staggered cubes with a 25% packing density, representing an idealized infinite city. This choice has been made to enable analyzing highly-converged statistics. The LES described in Sect. 2 is applied in a $16h \times 12h \times 8h$ computational domain, where cubical obstacles of dimension h are explicitly represented and where the mesh is refined close to the walls so as to resolve the viscous sublayer. A dynamic Smagorinsky SGS model (Germano et al., 1991) is specifically implemented in OpenFOAM to allow the model coefficient to vary within this highly heterogeneous flow. In Sect. 3, LES results are discussed and compared to literature data, including mean profiles up to the second-order momentum and turbulent spectra. Among the wind tunnel data, recent experiments performed in the LHEEA wind tunnel (Centrale Nantes Laboratory) provide a new dataset for assessing numerical simulations. Section 4 evaluates the TKE budget through a joint analysis with the wind tunnel measurements recorded by Blackman et al. (2017); also, a detailed analysis of TKE production is proposed via an in-depth description of its 3D organization. The final section collates the main outcomes and findings of this work.

2 Numerical Approach

2.1 The Governing Equations

The present LES is performed using the filtered Navier-Stokes equations for incompressible flows, as defined by the continuity equation:

$$\frac{\partial \widetilde{u}_i}{\partial x_i} = 0, \tag{1}$$

and the conservation of momentum equation:

$$\frac{\partial \widetilde{u}_i}{\partial t} + \frac{\partial \widetilde{u}_i \widetilde{u}_j}{\partial x_j} = -\frac{1}{\rho}\frac{\partial \widetilde{p}}{\partial x_i} + \frac{\partial}{\partial x_j}(\nu \frac{\partial \widetilde{u}_i}{\partial x_j} - \tau_{ij}), \tag{2}$$

where $\widetilde{u_i}$ (for $i = 1, 2, 3$) are the filtered velocity components; $\widetilde{p}$ is the filtered pressure, ρ the reference density, ν the kinematic viscosity, and $\tau_{ij} = \widetilde{u_i u_j} - \widetilde{u}_i \widetilde{u}_j$ the SGS stress tensor. The LES is carried out by means of a finite-volume method within the framework of the open-source C++ library OpenFOAM® 2.4.0 using MPI for interprocessor communication. The equations are solved in space according to a second-order central scheme, while the temporal integration is performed by a second-order backward implicit scheme.

2.2 **The Dynamic Smagorinsky Subgrid-scale Model**

LES results are known to be sensitive to the choice of SGS model, especially in the vicinity of walls where small-scale structures are prevalent. The well-known Smagorinsky (1963) model, widely employed in atmospheric flow research (Xie et al., 2008; Boppana et al., 2010), assumes a local equilibrium of turbulence at small scales where shear production and dissipation are in balance. In this model, the deviatoric part of the SGS stress tensor is defined as:

$$\tau_{ij} - \frac{1}{3}\tau_{kk}\delta_{ij} = -2\,\nu_{sgs}\,\widetilde{S_{ij}}, \tag{3}$$

where:

$$\widetilde{S_{ij}} = \frac{1}{2}\left(\frac{\partial \widetilde{u_i}}{\partial x_j} + \frac{\partial \widetilde{u_j}}{\partial x_i}\right) \tag{4}$$

is the resolved strain rate tensor and the SGS kinetic viscosity ν_{sgs} is modeled as:

$$\nu_{sgs} = (C_S \widetilde{\Delta})^2 |\widetilde{S_{ij}}|, \tag{5}$$

where $\widetilde{\Delta} = \sqrt[3]{\Delta x \Delta y \Delta z}$ is the grid-filter width, C_S the model coefficient, and $|\widetilde{S_{ij}}| = \sqrt{2\widetilde{S_{ij}}\widetilde{S_{ij}}}$. According to the Smagorinsky model, the isotropic part of the SGS stress tensor, which corresponds to the SGS energy, is not modeled but instead included in the pressure term of Eq. 1 so-called modified pressure (Calmet and Magnaudet, 1997; Tomas et al., 2016). In the flow regions where the SGS energy is strong, this modified pressure may vary significantly from the original pressure. In the following, the modified pressure values at the walls will be used to compute the drag force (Sect. 2.3). These values are expected to be close to the pressure values since the SGS energy is weak in the viscous sublayer. The modified pressure also serves to evaluate pressure transport in the TKE budget (Eq. 9), which involves the fluctuating part of the modified pressure. No evidence suggests that the SGS energy fluctuations would be negligible compared to the pressure fluctuations; nonetheless, we expect that this approximation will not exert undue influence on the statistical results.

The model coefficient C_S is typically prescribed to be a constant of a value ranging from 0.1 to 0.2 depending on the flow type. This *ad hoc* value, combined with the formulation of ν_{sgs}, prevents the model from simulating energy backscatter and results in an overestimation of modeled near-wall viscosity

194 if no damping is applied. To overcome this drawback, Germano et al. (1991)
195 proposed a dynamic procedure allowing for the model coefficient to be locally
196 computed. In this approach, a test-filter $\widehat{\widetilde{G}} = \widehat{G}\,\widetilde{G}$ is defined with a charac-
197 teristic width of $\widehat{\widetilde{\Delta}} = a \times \widetilde{\Delta}$. The momentum equation (Eq. 2) filtered with $\widehat{G}$
198 introduces a new SGS stress tensor, $T_{ij} = \widehat{\widetilde{u_i}\widetilde{u_j}} - \widehat{\widetilde{u}_i}\widehat{\widetilde{u}_j}$, which is an unknown
199 as well as τ_{ij}. In the dynamic Smagorinsky model the deviatoric part of the
200 SGS stress tensors at both the grid- and test-filter scales is modeled similarly
201 to Eqs. 3 and 5, in assuming that model coefficient C remains independent of
202 the filter scale:

$$\tau_{ij} - \frac{1}{3}\tau_{kk}\delta_{ij} = -2\,C\widetilde{\Delta}^2|\widetilde{S_{ij}}|\,\widetilde{S_{ij}}, \tag{6}$$

203 and

$$T_{ij} - \frac{1}{3}T_{kk}\delta_{ij} = -2\,C\widehat{\widetilde{\Delta}}^{\,2}\,|\widehat{\widetilde{S_{ij}}}|\,\widehat{\widetilde{S_{ij}}}. \tag{7}$$

204 The algebraic identity of Germano et al. (1991) defines the tensor $\mathscr{L}_{ij}$ as:

$$\mathscr{L}_{ij} = T_{ij} - \widehat{\tau_{ij}} = \widehat{\widetilde{u_i}\widetilde{u_j}} - \widehat{\widetilde{u}_i}\widehat{\widetilde{u}_j}, \tag{8}$$

205 which can be calculated explicitly by applying the filter $\widehat{G}$ to the resolved
206 velocity field. From Eqs. 6, 7, and 8, the following can be written:

$$\mathscr{L}_{ij} - \frac{1}{3}\mathscr{L}_{kk}\delta_{ij} = CM_{ij},$$

207 where $M_{ij} = -2\,\widetilde{\Delta}^2(a^2\,\widehat{|\widetilde{S_{ij}}|\,\widetilde{S_{ij}}} - \widehat{|\widetilde{S_{ij}}|\widetilde{S_{ij}}})$ with $a = 2$ in the present study.
208 As suggested by Lilly (1992), the dynamic coefficient C is computed at each
209 time step and at each computational cell using a least-squares method, through
210 the relation:

$$C = \frac{\mathscr{L}_{ij}\,M_{ij}}{M_{ij}\,M_{ij}}.$$

211 An appropriate SGS model is necessary to ensure an accurate numeri-
212 cal simulation, especially when analyzing flow close to a solid boundary. The
213 dynamic approach has been successfully used for simple flows such as plane
214 channel flows or recirculating flows (Calmet and Magnaudet, 1997; Zang et al.,
215 1993). It is unquestioned that the advantage of the dynamic Smagorinsky
216 model lies in its ability to consider the local change in model coefficient as il-
217 lustrated in Fig. 1. However, this dynamic procedure may locally induce large
218 negative values of the model coefficient C, giving rise to numerical instabili-
219 ties. In order to avoid this problem, total viscosity $(\nu + \nu_{sgs})$ is forced to be
220 locally a non-negative value. This method, called "clipping", can be found in
221 Calmet and Magnaudet (1997) and Ferziger et al. (2002).

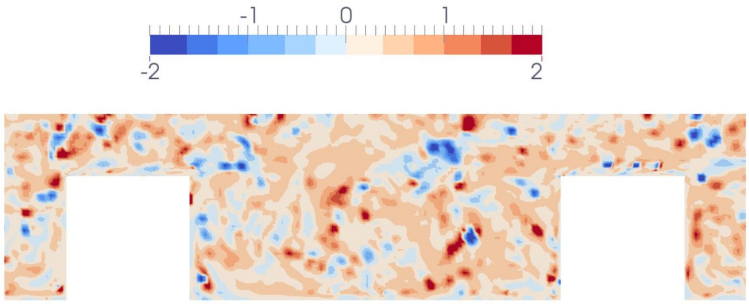

Fig. 1 Snapshot of the normalized dynamic Smagorinsky variable C/C_S^2 in a vertical plane with $C_S = 0.175$.

2.3 **Simulation Set-up**

Figure 2 shows the computational domain of dimension $16h \times 12h \times 8h$ in the streamwise (x), spanwise (y) and vertical (z) directions, respectively. This domain was chosen with reference to Coceal et al. (2007b) who successfully performed a DNS of the flow over an urban-like canopy. The floor is covered by a staggered array of cubes of uniform height (h) and a packing density of $\lambda_p = 25\%$.

Free-slip conditions are set at the top boundary of the domain, while no-slip conditions are prescribed at the floor and on all obstacle surfaces. Periodic boundary conditions are imposed in the spanwise and streamwise directions to simulate an infinite array of cubes. The flow is driven by a longitudinal pressure gradient adjusted at each time step to maintain a flow rate speed of 3.5 m s^{-1}. The Reynolds number (Re), based on both the velocity at the top of the domain and the domain height ($8h$), equals about $Re = 50,000$ and the friction Reynolds number, based on friction velocity u_τ and h is $Re_\tau = u_\tau h/\nu = 500$. The friction velocity u_τ is derived from the time-averaged total drag force (F) through the relation $u_\tau = \sqrt{\tau\,/\,\rho}$, with $\tau = F/A$ and $A = 16h \times 12h$, the total plane area. The total drag force is the sum of the pressure drag on the cubes, friction drag on the cubes and friction drag on the ground, with these contributions representing approximately 95%, 3.8% and 1.2 % of the total drag, respectively. The simulation details are summarized in Tab. 1.

Table 1 Main simulation parameters.

Array type	λ_p	$L_x \times L_y \times L_z$	h	u_τ	z_0	d	Re_τ	Re
Staggered	0.25	$16h \times 12h \times 8h$	0.02 m	0.40 m s^{-1}	$0.07h$	$0.74h$	500	50,000

Mesh size is an important parameter since, along with the considered Reynolds number, it determines both the size of the resolved eddies and the

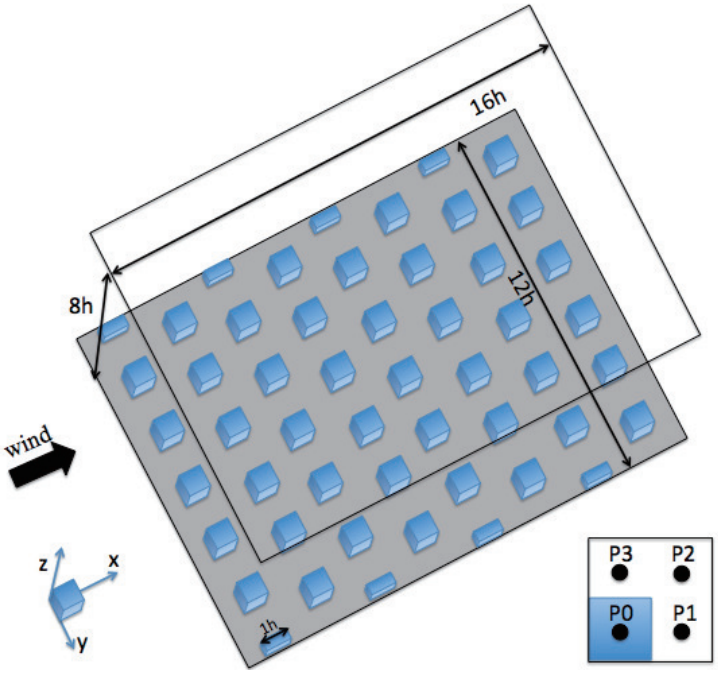

Fig. 2 View of the computational domain, where h is the cube height.

ability to account for large velocity gradients occurring near the walls. In comparing the numerical results they obtained with a grid spacing of $\Delta = h/32$ and $\Delta = h/64$, Coceal et al. (2006) concluded that simulations over a cubic geometry are generally resolved quite well with $\Delta = h/32$. Xie and Castro (2006) also pointed out that an LES using $\Delta = h/32$ was able to capture the vertical gradient of the vertical velocity fluctuations near the top of the canopy. In their DNS, using a grid spacing of $\Delta = h/32$ Coceal et al. (2007b) also obtained results in good agreement with wind-tunnel data (Cheng and Castro, 2002). In the present configuration, a sensitivity analysis (not presented here) indicated that a grid spacing of $\Delta = h/32$ fails to resolve the flow gradients that occur within the viscous sublayer near surfaces, especially at the top of the cubes. Tomas et al. (2016) suggested using a vertical grid spacing of $\Delta = h/100$ in this region. Here, in the absence of a wall model, a vertical grid spacing of $h/128$ at the top of the cubes makes it possible for three mesh layers to be below $z^+ = \frac{zu_*}{\nu} = 5$ (with u_* the local friction velocity above a cube, determined in the viscous sublayer by $u_*^2 = \nu\frac{\partial \overline{u}}{\partial z}$). This set-up is sufficient to resolve the viscous sublayer in this region which proves to be important for developing the shear layer downstream of the cube.

The final mesh configuration is based on a homogeneous $\Delta = h/32$ mesh spacing below $z = 1.5h$ with a refinement of $h/64$ on all surfaces and down to $h/128$ at the top of the cubes. Above $z = 1.5h$, the mesh keeps the same size

in the horizontal directions but gradually stretches in the vertical direction. The average vertical mesh size is $h/10$ in the region $1.5 < z/h < 5$ and $h/2$ in the region $5 < z/h < 8$ with a maximum value of $2h/3$ at the top of the domain. The final mesh is non-uniform and contains roughly 28 million cells. The approximate number of cells in the streamwise, spanwise and vertical directions is $N_x = 520$, $N_y = 410$, and $N_z = 110$, respectively.

The simulation is performed with a constant time step of $\Delta t = 0.00076T$ where $T = h/u_\tau$ can be interpreted as "the eddy turnover time for the largest eddies shed by the cube" (Coceal et al., 2006). An initial simulation is run on a period of $300T$ in order to reach a statistical steady state; this time period is longer than the duration reported in previous studies (Coceal et al., 2006). The simulation is then pursued for $200T$ in order to compute the high-order statistics necessary to determine the TKE budget terms. Xie and Castro (2006) argued that $80T$ is sufficient for statistical convergence and even observed that the variation in statistical data throughout the RSL was generally rather small after an averaging duration in excess of $20T$. Coceal et al. (2007a) and Coceal et al. (2007b) chose $100T$ for their simulation in the same computational domain as for the present work. In more recent studies, Tomas et al. (2016) opted for $56T$ yet used inlet/oulet conditions instead of periodic boundary conditions, while Castro et al. (2017) settled on $710T$ for the statistics collection step. In the present study, the statistics obtained over a duration of $200T$ are observed to converge at least up to the third-order moments.

In the following discussion, time averaging of the resolved fields will be denoted by an over-bar ($\overline{..}$). Fluctuation with respect to this average will be denoted by a prime symbol such that the resolved velocity component can be decomposed as $\widetilde{u_i} = \overline{u}_i + u_i^{'}$. Hereafter, u, v and w denote the streamwise, spanwise and vertical velocity components, respectively.

3 Assessment of the Numerical Approach

The mean vertical profiles of both the longitudinal velocity and the Reynolds shear stress components are investigated at four locations ($P0$, $P1$, $P2$ and $P3$, as indicated in Fig. 2) to be compared to various experimental and numerical data in the literature. The experimental work of Castro et al. (2006) has been used to draw comparisons and enriched by recent experimental datasets from the LHEEA atmospheric wind tunnel (Nantes, France), i.e.: the Laser Doppler Velocimetry (LDV) dataset from Herpin et al. (2018), and two datasets generated from Particle Image Velocimetry (PIV) by Blackman and Perret (2016) and by Blackman et al. (2017). Note that in order to be directly compared with numerical results, PIV datasets must undergo two modifications relative to what has been reported in the cited papers: 1) vertical profiles are extracted here at points $P1$, $P2$ and $P3$ without spatial averaging, and 2) experimental data are normalized here by the friction velocity obtained from drag force measurements (see Sect. 2.3 above and Herpin et al. (2018): viscous drag was not measured during this experiment). This was the alternative used instead

of the Reynolds shear stress values in the region where it remains nearly constant. Results are also compared to the direct numerical simulations (DNS) by Coceal et al. (2007b).

3.1 **Mean Streamwise Velocity**

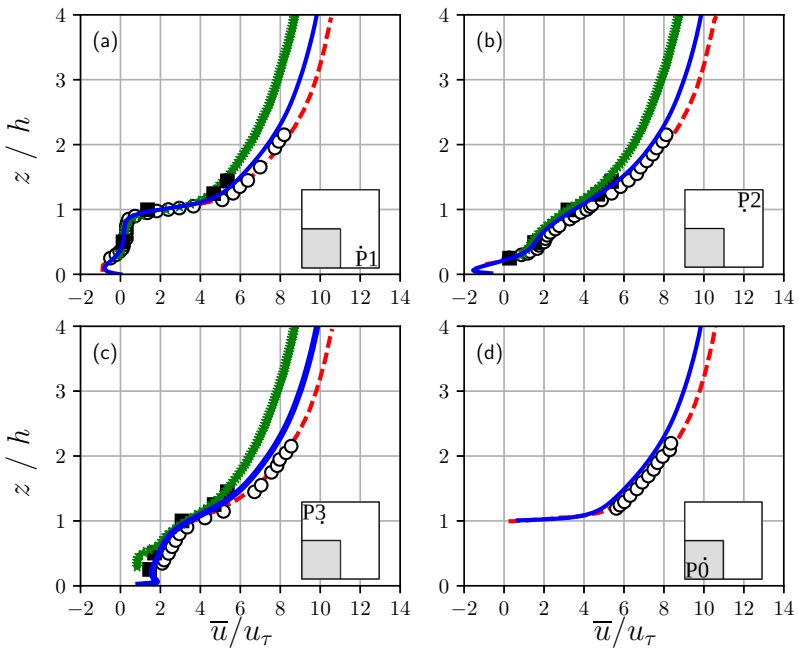

Fig. 3 Vertical profiles of the mean streamwise velocity at locations $P1$ (**a**), $P2$ (**b**), $P3$ (**c**), $P0$ (**d**). Blue solid line: LES computations; Red dashed line: DNS data from Coceal et al. (2007b); Circles: wind-tunnel data from Castro et al. (2006); Squares: wind-tunnel data from Herpin et al. (2018); Stars: PIV data from Blackman et al. (2017).

Figure 3 shows the vertical profiles of the mean streamwise velocity component normalized by the friction velocity (u_τ). LES results (in blue in Fig. 3) are in good agreement with both DNS data from Coceal et al. (2007b) and wind-tunnel measurements performed by Castro et al. (2006) at the four locations presented. This observation is equally valid inside the canopy and up to $z/h = 4$.

Inside the canopy and in the vicinity of the cubes ($z/h \leq 1.25$) results are also in good agreement with the wind-tunnel output from Herpin et al. (2018)

using LDV and from Blackman et al. (2017) using PIV. Let's note that in the present case, like in Coceal et al. (2007b), the cube height to boundary-layer height ratio equals $h/\delta = 12.5\%$ which is close to the configuration by Castro et al. (2006), i.e. $h/\delta = 13\%$. This ratio however differs by a factor of 2.75 times higher than in both Herpin et al. (2018) and Blackman et al. (2017), for whom $h/\delta = 4.5\%$. The widening differences with increasing height may be attributed to differences in the relative boundary layer height.

The variety of mean velocity profiles observed at different locations inside the canopy illustrates the inhomogeneity of the flow induced by the presence of cubes. The mean reverse flow observed in the numerical results in the lower part of the canopy downstream of a cube at $P1$ (Fig. 3b) and upstream of a cube at $P2$ (Fig. 3a) demonstrates the presence of time-averaged recirculation structures on both the windward (upstream recirculation) and leeward (wake recirculation) sides of the cube. The presence of strong local velocity gradients at $z = h$ (see Figs. 3a-c) indicates a strong shear layer.

3.2 **Reynolds Stress Components**

Figures 4 and 5 show the turbulent characteristics of the flow normalized by u_τ at locations $P1$, $P2$ and $P3$. These results display the resolved contribution, except for the Figs. 4a, c, e, in which the SGS contribution has been added to the resolved Reynolds shear stress, in this case, accounting for up to 3% or 4% of the total.
The turbulent shear stress ($-\overline{u'w'}$) above the canopy and down to $z/h = 0.2$ at $P1$ and $P2$ corresponds fairly well to both the DNS of Coceal et al. (2007b) and wind-tunnel data (Figs. 4a, c). Upstream of the cube ($P2$), a local maximum is observed in our LES results at $z/h = 0.1$ (Fig. 4c). Xie and Castro (2006) recorded the same observation and suggested as a cause the viscous sublayer which had been well resolved close to the wall at this position. However, at $P2$ for $z/h = 0.1$, a reverse flow is observed in Fig. 3b. A peak is also identified in the standard deviation of the longitudinal velocity component σ_u (Fig. 5c). This peak is more likely to be correlated with the upstream recirculation area located upwind of the cube (more details about this area are given in Sect. 4, see also Fig. 11a).

For the positions presented, the maximum Reynolds shear stress is located near the cube height in both simulations and experiments. In the wake of the cube (at $P1$) the numerical simulations underestimate this maximum in comparison to experimental data of Castro et al. (2006) while the PIV results by Blackman and Perret (2016) yield the lowest maximum (Fig. 4a). Discrepancies are also found for the standard deviation of the vertical velocity component σ_w: the peak of σ_w obtained with numerical simulations lies between the experimental results (Fig. 4b). Similar observations were recorded by Reynolds and Castro (2008) who pointed out two main reasons explaining

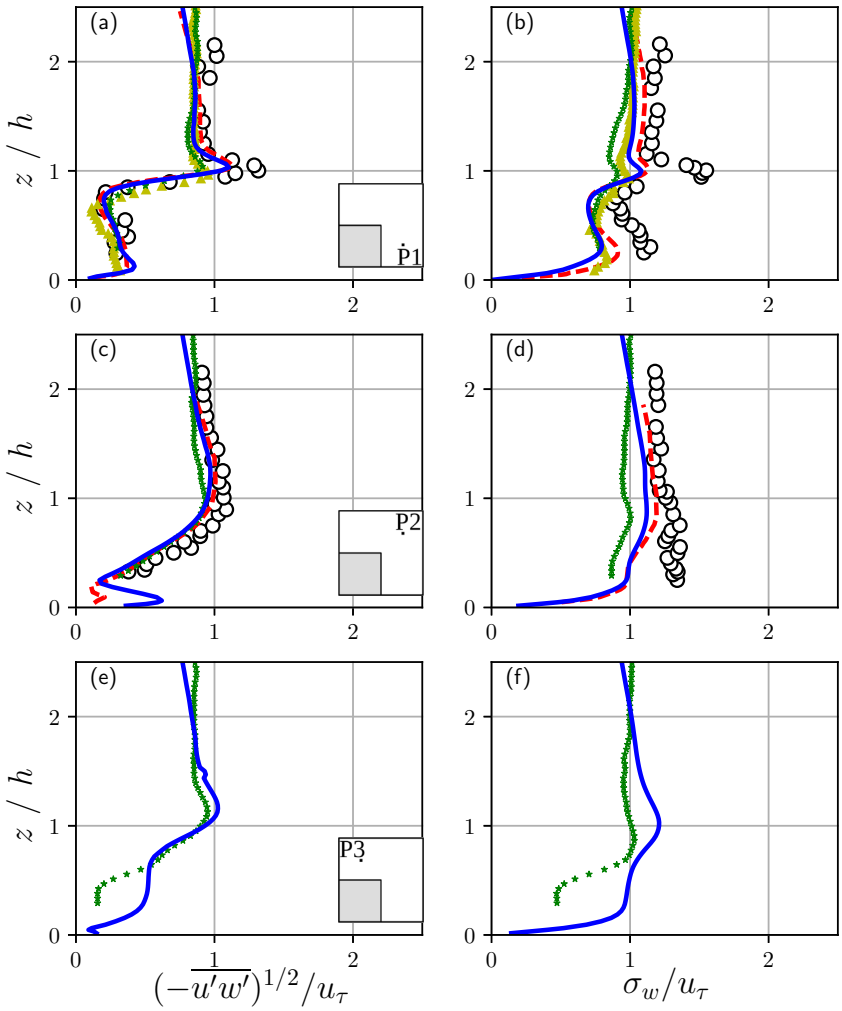

Fig. 4 Vertical profiles of normalized Reynolds shear stress and vertical velocity standard deviation at $P1$ (a, b), $P2$ (c,d) and $P3$ (e, f). Solid line: LES; Dashed line: DNS from Coceal et al. (2007b); Circles: wind-tunnel data from Castro et al. (2006); Triangles: wind-tunnel data from Blackman and Perret (2016); Stars: wind-tunnel data from Blackman et al. (2017).

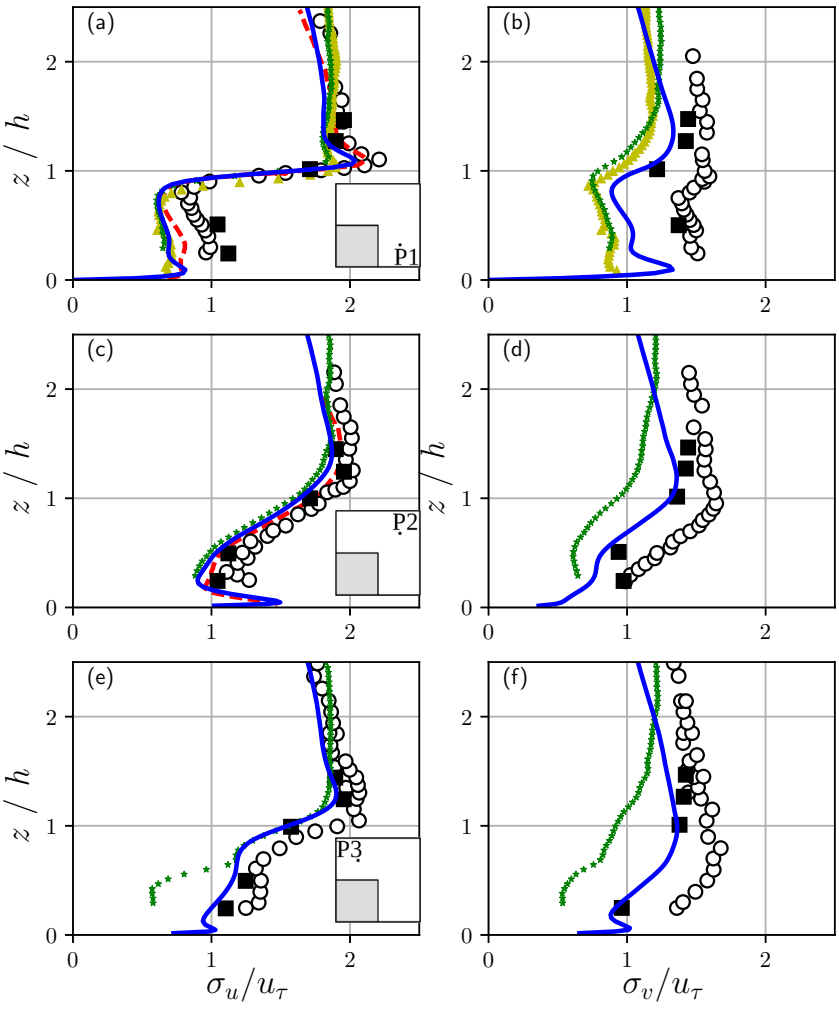

Fig. 5 Vertical profiles of the standard deviation of the streamwise and spanwise velocity components at $P1$ (a, b), $P2$ (c, d) and $P3$ (e, f). Solid line: LES; Dashed line: DNS from Coceal et al. (2007b); Circles: wind-tunnel data from Castro et al. (2006); Squares: wind-tunnel data from Herpin et al. (2018); Triangles: wind-tunnel data from Blackman and Perret (2016); Stars: wind-tunnel data from Blackman et al. (2017).

the differences in the peaks of $(-\overline{u'w'})$ and σ_w. The first is based on the h/δ ratio. These authors found that for $h/\delta < 10\%$, the Reynolds stresses reach a minimum asymptotic value, which means that the greater the h/δ value, the higher the shear stress peaks. This finding is replicated here in Fig. 4, where the datasets contain very different values of h/δ (see Sect. 3.1). The second reason is tied to resolution, whereby a coarser resolution tends to smooth the peak value (Scarano and Riethmuller, 2000). LDV measurements conducted by Castro et al. (2006) have a vertical resolution of approximately $0.015h$, while the PIV resolution by Blackman et al. (2017) is around $0.038h$. PIV is therefore expected to smooth the local peaks of shear components as compared to LDV data. According to a method introduced by Tomas et al. (2016), a rough evaluation of the ratio of shear stress effectively resolved by PIV to total shear stress has been derived; it is based on the work of Scarano and Riethmuller (2000), wherein the percentage of resolved velocity is estimated as a function of the ratio between PIV interrogation window size and the integral length scale. When applied to the works of Blackman and Perret (2016) and Blackman et al. (2017), at P1, for $z = h$, the PIV resolved part is estimated at 94% and 90%, respectively. These results are to be treated with caution since the work of Scarano and Riethmuller (2000) is based on idealized PIV images. In LES, the resolution near $z = h$ is approximately $0.031h$, which is indeed finer than PIV but still twice as large as the LDV measurements. This explanation, also proposed by Eisma et al. (2018) is correlated with the observations depicted in Figs. 4a, b.

At point $P2$, the experimental data from Castro et al. (2006) and Blackman et al. (2017) are also available for comparison with the numerical results of σ_w (Fig. 4d). Both DNS and LES values of σ_w fall between the two experimental datasets.

At point $P3$, the vertical profiles of $(-\overline{u'w'})$ and σ_w are rarely reported in the literature. The LES shear stress profile is in rather good agreement with PIV data above the canopy and down to $z/h = 0.6$. Below this level, large discrepancies are observed between LES results and PIV data (Fig. 4f). The vertical profile of σ_w shows large discrepancies at all heights (Fig. 4f), but no experimental data other than Blackman et al. (2017) are available for comparison.

The standard deviation of streamwise (σ_u) and spanwise (σ_v) velocity components are presented in Fig. 5. LES results indicate that the accuracy in simulating σ_u is close to that of the DNS (Coceal et al., 2007b) at $P1$ and $P2$. At $P1$, below $z/h = 1$, numerical data are in good agreement with PIV data (Fig. 5a) yet significantly lower than results from use of the LDV technique. In such a wake region, the lack of spatial resolution probably explains these differences. At $P2$ and $P3$ (Figs. 5c, e) numerical results closely match the LDV data from Herpin et al. (2018).

The standard deviation of the spanwise velocity (σ_v) is undoubtedly the most difficult Reynolds stress-tensor component to measure and simulate. In stereo-PIV measurements, the spanwise velocity component is reconstructed

from the in-plane displacement; consequently, the attenuation of velocity fluctuations is expected to be greater than for the streamwise and vertical velocity components. Large discrepancies can be observed when comparing the results obtained in the various experiments (Figs. 5b, d, e). The LES however seems to provide the right trend in the profile of σ_v and is in quite good agreement with the wind-tunnel data from Herpin et al. (2018) at $P2$ and $P3$, as well as at $P1$ above and inside the canopy.

From this analysis, it is clear that an assessment of the numerical method cannot be based on a single experimental dataset. The detailed reason why the various experimental approaches lead to different results lies beyond the scope of the present work. Nonetheless, the comparisons presented in this section do demonstrate that the overall agreement between our LES results and available data, including DNS, is highly satisfactory for both the first- and second-order moments.

3.3 **Energy Spectrum**

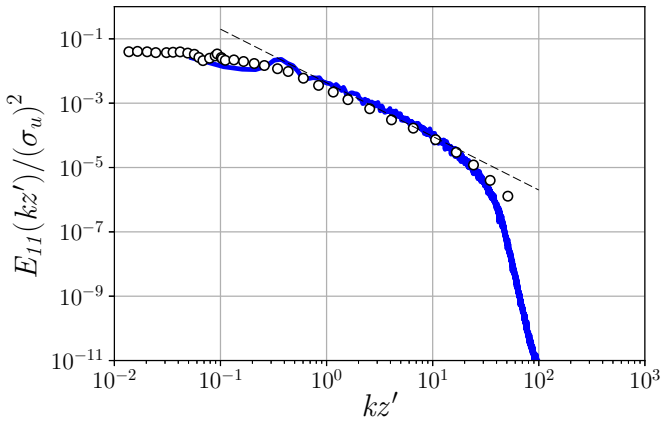

Fig. 6 Turbulent spectra of the axial velocity component $E_{11}(kz')$ at $P2$ for $z/h = 1.62$ from LES (solid blue line), compared with wind-tunnel data (circles) from Castro et al. (2006). The black dashed line represents the -5/3 slope.

In Fig. 6, the temporal spectrum $E_{11}(kz')$ of the streamwise velocity component above the cubes ($z/h = 1.62$) is shown at $P2$ and compared with wind-tunnel data from Castro et al. (2006). This spectrum has been computed from six time series of the longitudinal velocity fluctuation lasting $45T$ and sampled at 2 kHz. The wave-number k is defined as $k = 2\pi f/\overline{u}$, with f being the frequency. The variable z' is defined as $z' = z - d$, with d denoting the zero-plane displacement estimated as the height at which the total drag

is acting. According to the method derived by Jackson (1981), d is computed by:

$$d = \frac{\int_0^h zD(z)\,dz}{\int_0^h D(z)\,dz},$$

where $D(z)$ is the total drag force profile including pressure and viscous forces within the canopy (See Sect. 2.3). This method has been widely debated because fitting the logarithmic profile with the resulting value of d implies large discrepancies in the value of the von Kármán's constant κ (Coceal et al., 2007b). In our simulation however, this method generally yields acceptable values of $d = 0.74h$ and $\kappa = 0.4$.

Assuming that the smallest resolved eddies in the streamwise direction are sized 4Δ, $k_{max}z' = \frac{2\Pi}{4\Delta}z' \approx 44$ can be defined as the highest relevant wave number. Due to a sampling frequency of 2 kHz, values above $k_{max}z'$ exist but are irrelevant when considering the mesh resolution. Given that the size of the largest structures resolved in the simulation are of the order of the longitudinal length scale (L_x), $k_{min}z' = \frac{2\Pi}{L_x}z' \approx 0.34$ provides the lower limit of safe interpretation of the turbulent spectra. Data below k_{min} exist because the spectra have been computed from time series lasting $45T$, more than the turnover time under periodic conditions.

The simulated energy spectrum (Fig. 6) closely matches with the wind-tunnel data, and the inertial subrange is accurately captured ($-5/3$ slope, dashed line). The cutoff wave number of the LES ($k_{max}z'$) seems to lie at the boundary of the inertial subrange, meaning that at this location, the LES solves all the inertial subrange. The SGS dissipation of the dynamic Smagorinsky model should then be small, which will be confirmed in Sect. 4. As expected, for wave numbers greater than $k_{max}z'$, the energy of the small scales starts to drop faster in the simulation than in the experiment. For low wave numbers, the limited size of the LES domain is expected to lead to a poor simulation of the large structures, yet the energy deficit for $kz' < k_{min}z'$ is quite limited compared to wind-tunnel data.

4 Turbulence Kinetic Energy Budget

In order to further investigate the dynamics of turbulent flow in both the RSL and UCL, the budget of the TKE (defined as $\frac{1}{2}\overline{u_i'u_i'}$) is studied. From LES equations (Eqs. 1, 2, 4 and 6), and in assuming that the turbulent flow has reached a fully steady state, the TKE budget can be written as follows:

$$0 = \underbrace{-\overline{\mathrm{u}_j}\frac{\partial}{\partial x_j}\left(\frac{1}{2}\overline{u_i' u_i'}\right)}_{A} \underbrace{-\overline{u_i' u_j'}\,\overline{\mathrm{S}_{ij}}}_{P} \underbrace{-\frac{1}{2}\frac{\partial}{\partial x_j}\left(\overline{u_i' u_i' u_j'}\right)}_{T_r} \underbrace{-\frac{1}{\rho}\frac{\partial}{\partial x_i}\left(\overline{u_i' p'}\right)}_{T_p}$$
$$\underbrace{+\frac{\partial}{\partial x_j}\left(2\nu\,\overline{u_i' S_{ij}'}\right)}_{D_\nu} \underbrace{-2\nu\,\overline{S_{ij}' S_{ij}'}}_{\epsilon_r} \underbrace{-\frac{\partial}{\partial x_j}\left(\overline{u_i' \tau_{ij}'}\right)}_{T_{sgs}} \underbrace{+\overline{\tau_{ij}' S_{ij}'}}_{\epsilon_{sgs}}, \tag{9}$$

where A denotes advection by the mean flow, P production by shear, T_r turbulent transport by resolved velocity fluctuations, T_p transport by pressure fluctuations, D_ν viscous diffusion, ϵ_r resolved dissipation, T_{sgs} SGS transport, ϵ_{sgs} SGS dissipation, which represents the transfer of energy between the resolved-scale and the subgrid-scale through the cutoff, and $\tau_{ij}^{'} = \tau_{ij} - \overline{\tau_{ij}}$. Hereafter, the terms of the TKE budget normalized by u_τ^3/h will be provided for comparison and analysis. All contributions to the TKE budget are directly and individually computed during the simulation. A residual term is defined as the value needed on the r.h.s. of Eq. 9 to balance the TKE budget. This residual term (normalized by u_τ^3/h) is approximately -1 at $z = h$ and asymptotically tends to zero for $z > h$. For $z < h$, the residual lies in the range $[-2 : 0]$ (Fig. 8). Since the residual is always negative, this suggests that a destructive TKE term is missing in Eq. 9; this problem may be partially attributed to numerical approximation (second-order schemes in Navier-Stokes equation, linear interpolation applied to compute TKE terms at the cell center and computation of gradients in Eq. 9) that tend to smooth velocity gradients.

4.1 The Turbulence Kinetic Energy Budget in the Vicinity of a Cube

Figure 7 depicts all contributions to the TKE budget at positions $P0-3$. Note that D_ν is not represented because it remains very small at high Reynolds number flows.

At all locations, above the height $z/h = 1.5$, the shear production (P) and dissipation terms ($\epsilon = \epsilon_{sgs} + \epsilon_r$) are the major contributors to the TKE budget and tend to balance each other out with increasing height. At $P1$, P reaches a maximum just above the cubes (Fig. 7a), where shear stress is the highest (Fig. 4). The sharp peak then rapidly decreases both above and below $z/h = 1$. With the downwind distance from $P3$ to $P2$, the production peak decreases in intensity as the shear layer develops, becomes thicker and shifts slightly above $z/h = 1$ (see Fig. 7b, c).

Dissipation generally acts in mirror with production, at lower absolute values. The maximum $|P|/|\epsilon|$ ratios are found between $z/h = 1$ and $z/h = 2$, reaching 1.6, 6, 2.4, and 2.25 for $P0$ to $P3$, respectively. This trend indicates a strong contribution from other TKE budget terms in the area: turbulent transport, advection, and pressure transport. Extending higher above the cubes, the ratio

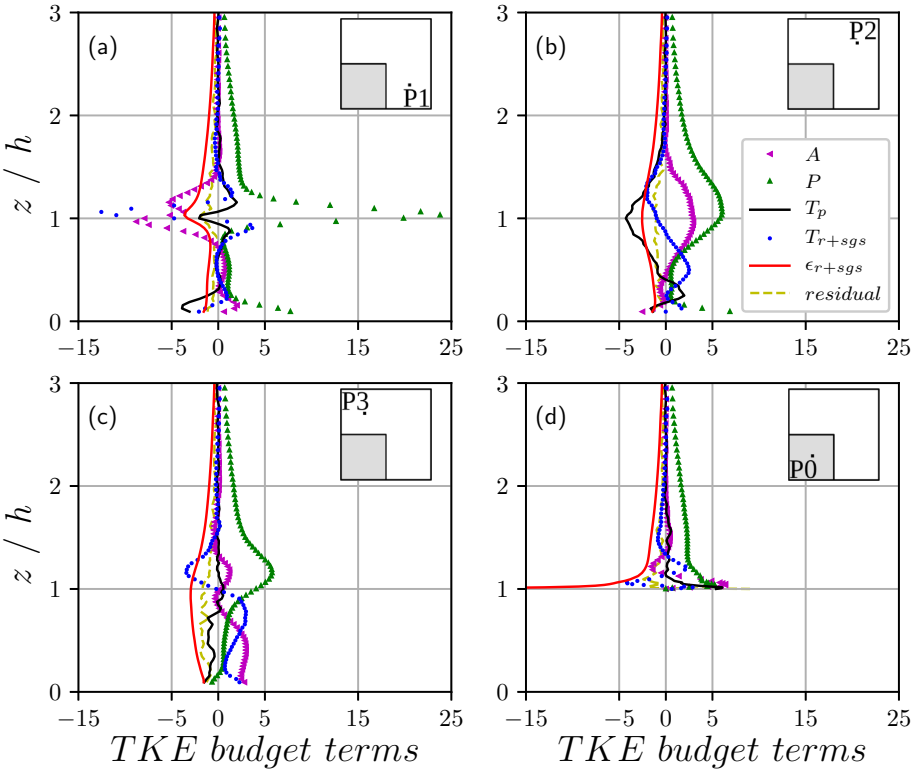

Fig. 7 Vertical profiles of TKE budget terms at locations (a) $P1$, (b) $P2$, (c) $P3$ and (d) $P0$, with all terms being normalized by u_τ^3/h.

decreases slowly and stabilizes at a quasi-equilibrium ($|P|/|\epsilon| = 1.1$). The two locations where dissipation is clearly greater than production are inside the canopy at $P3$ ($z/h < 1$) and at $P2$ ($0.6 < z/h < 0.2$).

In the simulation, the turbulent transport term of the TKE budget ($T_r + T_{sgs}$) is mostly resolved, as $T_{sgs}/(T_r + T_{sgs}) < 1\%$. At $P1$, turbulent transport is the major energy sink in the shear layer: $T_r + T_{sgs} < 0$ around $z/h = 1.05$. Just below and just above, turbulent transport is an energy source ($T_r + T_{sgs} > 0$ around $z/h = 0.9$ and $z/h = 1.2$). Turbulence transport transfers energy from the thin shear layer downwards inside the canopy and upwards into the roughness sublayer. Moving downwind, from $P3$ to $P2$, the region where turbulent transport acts as an energy sink is shifted to a higher altitude and broadens in agreement with the shear layer thickening. Just upstream of the cube (at $P2$), this region expands from $z/h = 1.5$ down to $z/h = 0.9$. At $P1$, turbulent transport acts with the same strength upwards and downwards

but, further downwind ($P3$ and $P2$), the energy transfer is clearly oriented downwards.

The transport by pressure fluctuations (T_p) acts similarly to the turbulent transport in front of the cube (Fig. 7a), by transferring energy both upwards and downwards. However, the contribution of T_p is much more significant in front of a cube (at $P2$) than behind (at $P1$). At $P2$, this contribution constitutes a major energy sink in the region between $z/h = 0.5$ and $z/h = 1.7$. The advection term (A) has a significant negative contribution in the shear layer downwind of the cube ($z/h = 1$, $P1$), where the mean flow is transferring TKE from $P1$ downwind. Further downwind, ($P2$ at $z/h = 1$), A is a TKE source, the mean flow brings TKE from the upstream. Inside the canopy, the contribution of advection is normally low, except at $P3$, where A is the major TKE source, and where TKE is transferred from the high TKE region situated between the two leading edges of the cubes downstream.

4.2 **Turbulence Kinetic Energy Budget Comparison**

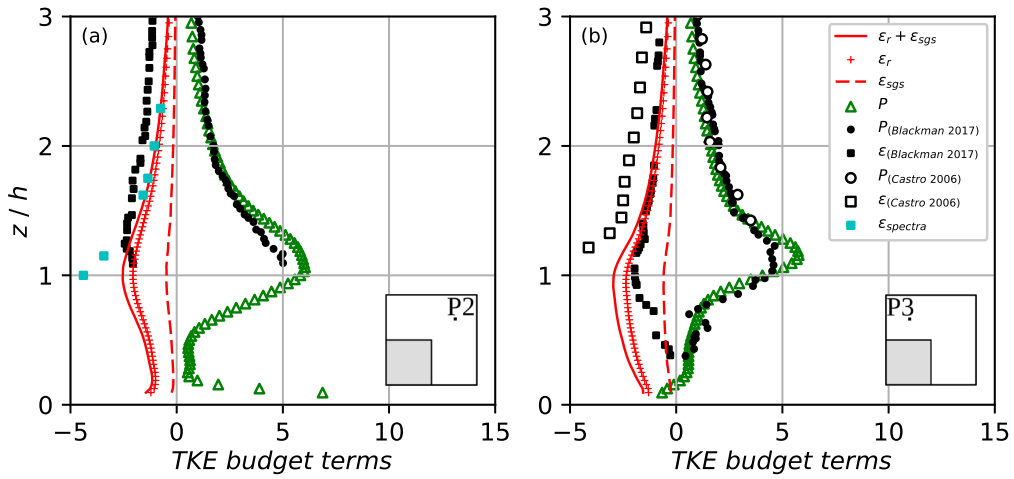

Fig. 8 Production and dissipation terms of the TKE budget vs. wind-tunnel data from Castro et al. (2006) and Blackman et al. (2017) at locations $P2$ (a) and $P3$ (b). All terms are normalized by u_τ^3/h.

Figure 8a shows the TKE budget computed from LES at locations $P2$ and $P3$ compared to the only two (to the best of the author's knowledge) experimental databases available for the TKE budget, i.e. PIV data from Blackman et al. (2017) and LDV data from Castro et al. (2006). For the sake of clarity, only production and dissipation are shown here.

The production profiles computed in this work are in very good agreement with experimental datasets both above and below $z = h$. However, at $z = h$, the computed P is higher than in the measurements found in Blackman et al. (2017) and displays a sharper peak (the production peak is not available in Castro et al. (2006)). The attenuation of velocity gradients by the PIV interrogation windows, as discussed in Sect. 3.2, offers a likely explanation. At both locations, for $z > h$, the total dissipation $(\epsilon_r + \epsilon_{sgs})$ modeled in the present work is slightly less than in the experimental datasets.

At position $P2$, assuming isotropic turbulence, the dissipation can be obtained from integrating of the turbulent spectra by computing:

$$\epsilon_{spectra} = 15\nu \int_0^\infty k_1^2 E_{11}(k_1) dk_1,$$

where k_1 is the wave number and $E_{11}(k_1)$ the one-dimensional wave number spectra (Perry et al., 1986). Above $z/h = 1.5$, $\epsilon_{spectra}$ compares well with the resolved dissipation rate ϵ_r calculated from Eq. 9, thus meaning that the grid is fine enough to resolve the local velocity gradients. In the shear layer, near $z/h = 1$, the isotropic turbulence hypothesis fails (see Figs. 4 and 5). Consequently, the calculation of $\epsilon_{spectra}$ is invalid, and lead to an overestimation of ϵ_r.

Inside the canopy, at $P3$ the computed total dissipation $(\epsilon_r + \epsilon_{sgs})$ is observed to be higher than in the experimental datasets of Blackman et al. (2017) for which dissipation rate may also depend on the way it was estimated (SGS model applied to PIV data).

4.3 **Production of Turbulence Kinetic Energy in the Vicinity of the Canopy**

The local TKE budget terms in Fig. 7 displayed great inhomogeneity in both the UCL and RSL. This section aims to both describe the spatial distribution of turbulence production P and interpret three-dimensional results from the LES calculation by showing 3D iso-contours (Fig. 9) and extracting 2D planes (Figs. 10 and 11). In the following, close to solid surfaces, two kinds of singular points are used for the description of the flow: saddles points (**S**) are where streamlines are converging/diverging denoting separation regions and node points or node lines (**N**) where streamlines are converging. Nodes are also called attachment points/lines or repelling points/lines.

Near the ground, three main areas produce TKE. The first (called P_1^+) is located at around $h/2$ upstream of a cube, near location $P2$ (as also observed in Fig. 8a). It is a crosswind-elongated ellipsoid with a length of approximately h where $P > 10$. This ellipsoid is visible in Figs. 10a and 11a. From Fig. 11a, it is clearly not horizontally oriented but rather tilted with its upwind part raised and its downwind part touching the ground. In examining the mean

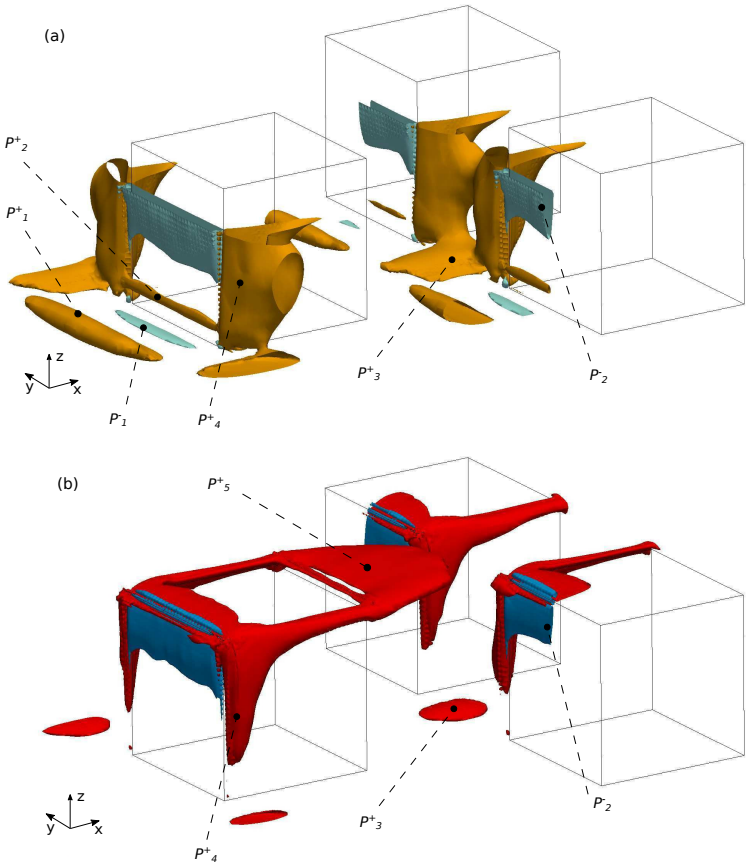

Fig. 9 Three-dimensional visualization of production, normalized by u_τ^3/h. For the sake of clarity, only three cubes are shown. (a) Close-up inside the urban canopy with iso-contours of $P = 10$ (orange) and $P = -10$ (light blue). Iso-contours are only shown below $z = 3h/4$. (b) View of production iso-contours $P = 25$ (red) and $P = -25$ (dark blue).

flow in this region, P_1^+ corresponds to the side of the strong clockwise upstream recirculation region located in front of the cube, where a high upward flow (normal to the wall) can be observed. This region corresponds to **S1** in Fig. 10a. A secondary P peak (P_2^+) is visible on the lower part of the windward face of the cube near **S4** (Figs. 9a and 11). It is an elongated spanwise structure located near the small secondary counterclockwise recirculation at the foot of the cube observed in Fig. 11. In this region, a wall-normal flow is also observed. Regions P_1^+ and P_2^+ are clearly linked to the near-wall mean flow upstream of a cube.

The third high production region close to the ground (P_3^+) is nearly circular in the horizontal plane and situated between the front faces of two cubes. Its center is located near **S2**, where the flow converges in the spanwise direction

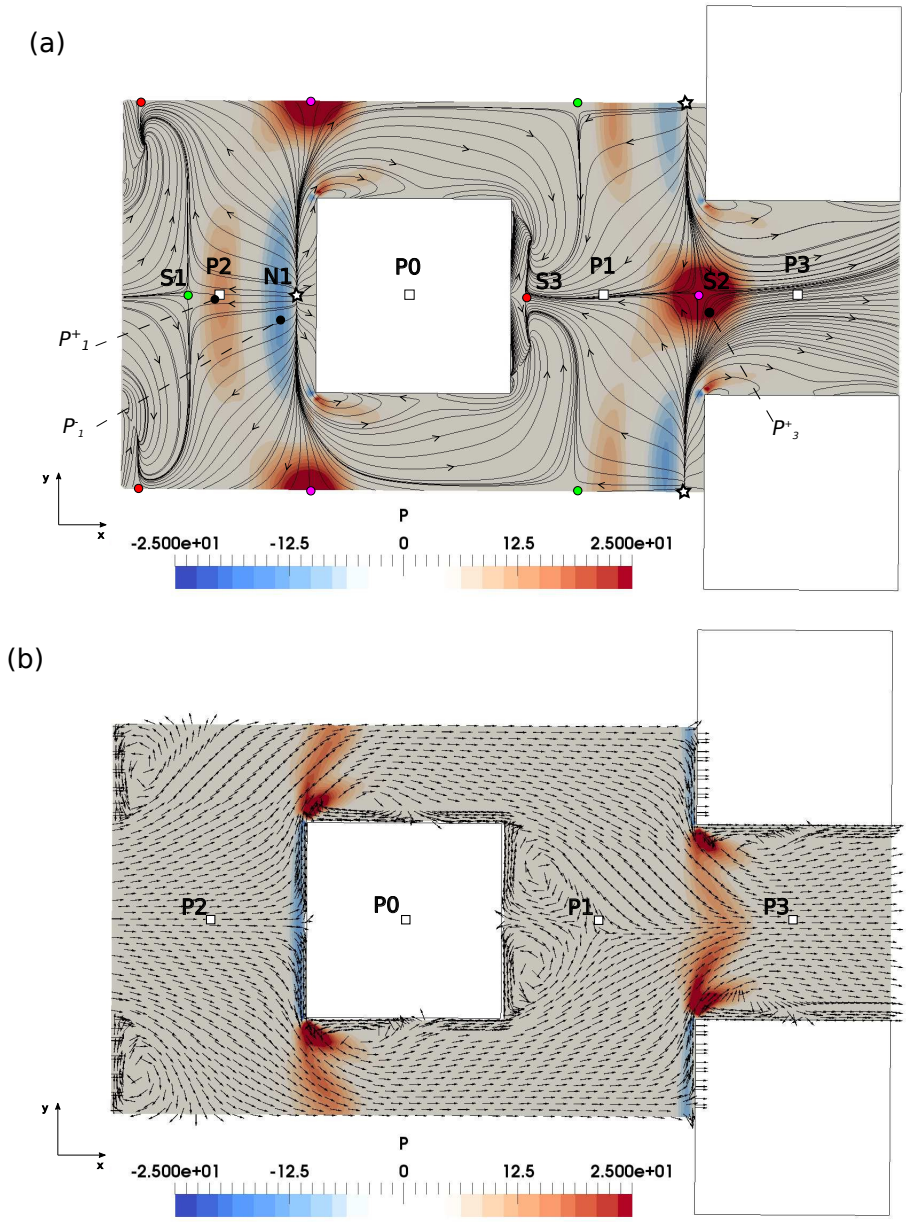

Fig. 10 Top view of the horizontal transect (X,Y) of production normalized by u_τ^3/h. Wind travels from left to right. (a) Near the ground ($z = h/40$) with planar velocity streamlines, where **S** and **N** locations stand for saddle point and node, respectively. (b) In the middle of the cube ($z = h/2$) with a mean velocity vector field. Vectors are of equal length in order to better visualize the flow structures.

due to the circumvention of the cubes (Fig. 10a, 9 and 11). Production here exceeds $P = 25$.

Extending up to $z = h/2$, P_3^+ merges with two high production regions (P_4^+) attached to the vertical edges of the windward face of the cube. These production regions at P_4^+ persist, strengthen with increasing height up to $z = h$. They also merge at $z = h/2$ in the spanwise space between two cubes (Figs. 10b and 9a). These regions correspond to the side of a lateral (xy)-plane recirculation zone along the vertical edge of the cube (visible in the vector field in Fig. 10b).

Other high production regions are observed (Fig. 9b) on the four top face edges. The strongest production area, P_5^+, starts from the trailing edge of a cube (downwind edge of the top face) and expands downwind to reach the second row of cubes with nearly $P > 25$ (as mentioned in Meinders and Hanjalić (1999)). Production intensity in this area which corresponds to the shear layer decreases with downwind distance from the cube and spreads in all directions but mainly upwards (see Fig. 11). Above $z = h/2$, all high production regions around the cube are clearly linked to flow separation on the sharp corners.

From the above description, we can state that high P regions are clearly correlated with separation regions. Close to solid surfaces, these separation regions are visualized by saddle points **S1**, **S2** and **S4**. These points are associated with tremendous outwards wall-normal motion. On cubes, they are located at the edges where flow separates. These flow regions may be linked to vortex shedding sources. Let us note that **S3** is also a saddle point, but not visible in Fig. 9 because the flow velocity is very low in this region.

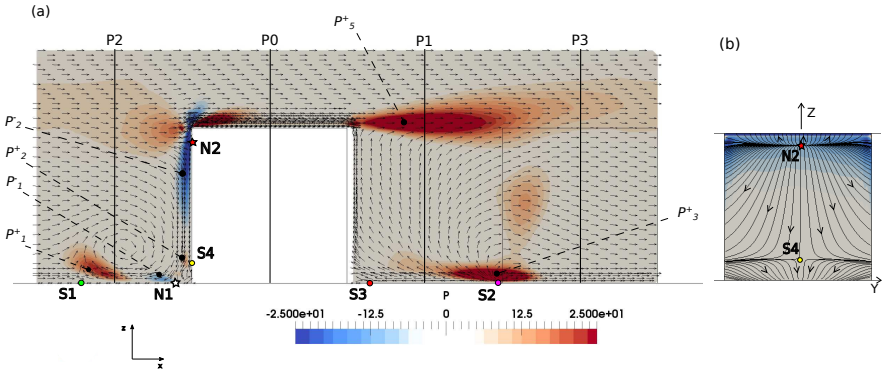

Fig. 11 (a) Vertical transects of production normalized by u_τ^3/h in the middle of the cube, with a projection of the mean velocity vector field. Vectors are of equal length in order to better visualize the flow structures. (b) Production on the wind face of a cube with wall streamlines.

The canopy flow also exhibits areas where P is negative, meaning that energy is extracted from turbulence and returned to the mean flow (Pope, 2001). For $z < h/2$, a spanwise elongated zone P_1^- with weak negative production ($P \approx -15$) is observed at the ground, near **N1** and parallel to P_1^+ (Figs. 10a and 11a). Point **N1** is a repelling line (Helman and Hesselink, 1989), representing a flow impinging on a surface. Here, it lies very close to the re-attachment zone situated between the large clockwise recirculation upwind of the cube and the secondary counterclockwise recirculation at the foot of the cube.
The region with the most highly negative production ($P < -25$), called P_2^-, starts at the cube's leading edge and extends downwards along the windward face of the cube with decreasing intensity to reach $P = -10$ at approximately $z = h/2$ (Figs. 11 and 9b). This region, near **N2** in Fig. 11 is also a repelling node (or line) where the mean turbulent flow is impacting the cube face and deflecting downwards. Instantaneously, it is likely that some of the vortices shed by leading edges of the previous cube (see instantaneous view in Coceal et al. (2006)) are being destroyed when impacting the subsequent cube, thus leading to a destruction of turbulence and an increase in the mean flow magnitude (down draft).
Similar regions of negative production were observed by Yakhot et al. (2006) around an isolated wall-mounted cube. They particularly decomposed production terms to explain its negative sign on the front face of the cube and linked them to mean flow features. However, in the present case, the spatial extent of P_1^- and its relative importance compared to P_2^- differ (in our work $P_2^- > P_1^-$). This difference can be attributed to the very different 3D organization of the turbulent flow, the dense staggered arrangement preventing the free expansion of the horseshoe vortex observed around an isolated cube.

5 Conclusion

In order to determine the turbulent mechanisms at play inside the UCL of an urban-like boundary layer, a large-eddy simulation was performed over a staggered array of cubes at $Re = 50,000$ ($Re_\tau = 500$). The simulation performed used a dedicated dynamic Smagorinsky subgrid scale model allowing for energy backscatter along with a $h/32$ mesh size and added refinements close to surfaces to resolve the viscous sublayers ($z^+ < 5$).

The high resolution of the LES presented in this work and the individual computation of each TKE budget terms made it possible to discuss the highly heterogeneous distribution of TKE terms inside the UCL. The role of advection, turbulent transport and pressure transport that are of secondary importance in the case of a flat plate away from the surface, are here clearly shown. Additionally, significant positive and negative values of turbulence production were found close to the ground surface.

This work showed, for the first time, that substantial TKE production areas in a staggered arrangement of cubes were located not just in the shear layer after a cube, as described in the literature, but also near surfaces. Sev-

eral locations on the ground and on some cube surfaces were identified where P is far from being negligible. Highly positive and negative production regions were observed, which allowed localizing where TKE is generated and where it returns to the mean flow. This finding is important to understanding how turbulence is generated and the boundary layer maintained in an urban-like canopy. This information can be valuable to build simplified urban canopy models. The TKE production process inside the urban canopy clearly differs from that of a flat plate and of an isolated wall-mounted cube. Although the turbulence production process is unsteady by its very nature, strong production areas could be identified at fixed locations other than in the shear layer or along the sharp edges of the obstacles.

In analyzing both high positive and negative production areas near surfaces, it is clear that each of them is related to distinctive features of the mean flow. High production areas are associated to saddle points. By definition, at a saddle point of a surface, there is a high convergence of the flow in the plane tangent to the surface. In the present configuration, the wall streamlines convergence is caused by the deflection of the flow around obstacles (as at S2) or by the presence of the recirculating area upwind of a cube (as at S1). The flow convergence results in both horizontal divergence and out-of-plane flow by virtue of mass conservation for incompressible flows. In a turbulent flow, this out-of-plane flow is very likely to produce TKE. Highly negative production areas close to surfaces are clearly correlated with node points. Repelling nodes (or repelling lines) are observed when the flow direction is normal to the surface as at the upwind face of the obstacle (N2) or at the junction of two recirculating flow regions (N1). Because of the divergence free condition it leads to a high divergence of the flow in the plane parallel to the surface. A node can be seen as a re-attachment zone. The TKE present in the flow is destroyed when impacting a surface and energy is transferred back to the mean flow resulting in a negative production of turbulence.

This finding is very likely to remain valid when changing the cube arrangement, array density or wind direction, meaning that high and low production areas near surfaces can simply be anticipated through analyzing the mean flow. To some extent, this statement may also be valid for configurations featuring square shapes such as buildings. Finally, the share of production at fixed locations compared to instantaneous advected vortices in the domain would provide an interesting subject to further analyze the turbulent production process.

Acknowledgements This work was granted access to the HPC resources of supercomputer CINES under the allocation 2017-A0020100132 made available by GENGI and of LIGER under the allocation 2017-E1703020 from Ecole Centrale de Nantes. The first author gratefully acknowledges help from Dr. Karin Blackman and Dr. Sophie Herpin as well as the financial support of the PhD scholarship from China Scholarship Council (CSC) under the grant CSC N° 20158070084. The authors want to thank the financial support of the French National Research Agency through the research grant URBANTURB N° ANR-14-CE22-0012-01.

References

Adrian RJ (2007) Hairpin vortex organization in wall turbulence. Physics of Fluids 19(4):041,301

Blackman K, Perret L (2016) Non-linear interactions in a boundary layer developing over an array of cubes using stochastic estimation. Physics of Fluids 28(9):095,108

Blackman K, Perret L, Calmet I, Rivet C (2017) Turbulent kinetic energy budget in the boundary layer developing over an urban-like rough wall using PIV. Physics of Fluids 29(8):085,113

Boppana VBL, Xie ZT, Castro IP (2010) Large-Eddy Simulation of Dispersion from Surface Sources in Arrays of Obstacles. Boundary-Layer Meteorology 135(3):433–454

Bou-Zeid E, Overney J, Rogers BD, Parlange MB (2009) The Effects of Building Representation and Clustering in Large-Eddy Simulations of Flows in Urban Canopies. Boundary-Layer Meteorology 132(3):415–436

Brooke JW, Hanratty T (1993) Origin of turbulence-producing eddies in a channel flow. Physics of Fluids A: Fluid Dynamics 5(4):1011–1022

Calmet I, Magnaudet J (1997) Large-eddy simulation of high-Schmidt number mass transfer in a turbulent channel flow. Physics of Fluids 9(2):438–455

Castro IP, Cheng H, Reynolds R (2006) Turbulence Over Urban-type Roughness: Deductions from Wind-tunnel Measurements. Boundary-Layer Meteorology 118(1):109–131

Castro IP, Xie ZT, Fuka V, Robins AG, Carpentieri M, Hayden P, Hertwig D, Coceal O (2017) Measurements and Computations of Flow in an Urban Street System. Boundary-Layer Meteorology 162(2):207–230

Cheng H, Castro IP (2002) Near wall flow over urban-like roughness. Boundary-Layer Meteorology 104(2):229–259

Cheng H, Hayden P, Robins A, Castro I (2007) Flow over cube arrays of different packing densities. Journal of Wind Engineering and Industrial Aerodynamics 95(8):715–740

Christen A, Rotach MW, Vogt R (2009) The Budget of Turbulent Kinetic Energy in the Urban Roughness Sublayer. Boundary-Layer Meteorology 131(2):193–222

Coceal O, Thomas TG, Castro IP, Belcher SE (2006) Mean flow and turbulence statistics over groups of urban-like cubical obstacles. Boundary-Layer Meteorology 121(3):491–519

Coceal O, Thomas TG, Belcher SE (2007a) Spatial Variability of Flow Statistics within Regular Building Arrays. Boundary-Layer Meteorology 125(3):537–552

Coceal O, Dobre A, Thomas TG, Belcher SE (2007b) Structure of turbulent flow over regular arrays of cubical roughness. Journal of Fluid Mechanics 589:375–519

Dwyer MJ, Patton EG, Shaw RH (1997) Turbulent kinetic energy budgets from a large-eddy simulation of airflow above and within a forest canopy. Boundary-Layer Meteorology 84(1):23–43

742 Eisma H, Tomas J, Pourquie M, Elsinga G, Jonker H, Westerweel J (2018)
743 Effects of a fence on pollutant dispersion in a boundary layer exposed to a
744 rural-to-urban transition. Boundary-layer meteorology 169(2):185–208
745 Ferziger JH, Perić M, Street RL (2002) Computational methods for fluid dy-
746 namics, vol 3. Springer
747 Finnigan J (2000) Turbulence in plant canopies. Annual review of fluid me-
748 chanics 32(1):519–571
749 Germano M, Piomelli U, Moin P, Cabot WH (1991) A dynamic subgridscale
750 eddy viscosity model. Physics of Fluids A: Fluid Dynamics 3(7):1760–1765
751 Giometto MG, Christen A, Meneveau C, Fang J, Krafczyk M, Parlange
752 MB (2016) Spatial Characteristics of Roughness Sublayer Mean Flow and
753 Turbulence Over a Realistic Urban Surface. Boundary-Layer Meteorology
754 160(3):425–452
755 Helman J, Hesselink L (1989) Representation and display of vector field topol-
756 ogy in fluid flow data sets. Computer (8):27–36
757 Herpin S, Perret L, Mathis R, Tanguy C, Lasserre JJ (2018) Investigation of
758 the flow inside an urban canopy immersed into an atmospheric boundary
759 layer using laser Doppler anemometry. Experiments in Fluids 59(5)
760 Hudson JD, Dykhno L, Hanratty T (1996) Turbulence production in flow over
761 a wavy wall. Experiments in Fluids 20(4):257–265
762 Inagaki A, Kanda M (2010) Organized structure of active turbulence over an
763 array of cubes within the logarithmic layer of atmospheric flow. Boundary-
764 layer meteorology 135(2):209–228
765 Jackson PS (1981) On the displacement height in the logarithmic velocity
766 profile. Journal of Fluid Mechanics 111:15
767 Kanda M, Moriwaki R, Kasamatsu F (2004) Large-eddy simulation of turbu-
768 lent organized structures within and above explicitly resolved cube arrays.
769 Boundary-Layer Meteorology 112(2):343–368
770 Kastner-Klein P, Rotach MW (2004) Mean Flow and Turbulence Charac-
771 teristics in an Urban Roughness Sublayer. Boundary-Layer Meteorology
772 111(1):55–84
773 Kim J, Moin P, Moser R (1987) Turbulence statistics in fully developed channel
774 flow at low reynolds number. Journal of fluid mechanics 177:133–166
775 Kono T, Tamura T, Ashie Y (2010) Numerical Investigations of Mean Winds
776 Within Canopies of Regularly Arrayed Cubical Buildings Under Neutral
777 Stability Conditions. Boundary-Layer Meteorology 134(1):131–155
778 Leonardi S, Castro IP (2010) Channel flow over large cube roughness: a direct
779 numerical simulation study. Journal of Fluid Mechanics 651:519
780 Lilly DK (1992) A proposed modification of the Germano subgridscale closure
781 method. Physics of Fluids A: Fluid Dynamics 4(3):633–635
782 Lyons S, Hanratty T, McLaughlin J (1989) Turbulence-producing eddies in
783 the viscous wall region. AIChE journal 35(12):1962–1974
784 Macdonald RW (2000) Modelling the mean velocity profile in the urban canopy
785 layer. Boundary-Layer Meteorology 97(1):25–45
786 Meinders E, Hanjalić K (1999) Vortex structure and heat transfer in turbulent
787 flow over a wall-mounted matrix of cubes. International Journal of Heat and

fluid flow 20(3):255–267
Monnier B, Goudarzi SA, Vinuesa R, Wark C (2018) Turbulent Structure of a Simplified Urban Fluid Flow Studied Through Stereoscopic Particle Image Velocimetry. Boundary-Layer Meteorology 166(2):239–268
Oke TR (1997) Urban environments. The surface climates of Canada pp 303–327
Perret L, Blackman K, Savory E (2016) Combining Wind-Tunnel and Field Measurements of Street-Canyon Flow via Stochastic Estimation. Boundary-Layer Meteorology 161(3):491–517
Perry A, Henbest S, Chong M (1986) A theoretical and experimental study of wall turbulence. Journal of Fluid Mechanics 165:163–199
Pope SB (2001) Turbulent flows. IOP Publishing
Raupach MR, Antonia RA, Rajagopalan S (1991) Rough-wall turbulent boundary layers. Applied mechanics reviews 44(1):1–25
Reynolds RT, Castro IP (2008) Measurements in an urban-type boundary layer. Experiments in Fluids 45(1):141–156
Rotach MW (1999) On the influence of the urban roughness sublayer on turbulence and dispersion. Atmospheric Environment 33(24):4001–4008
Roth M, Inagaki A, Sugawara H, Kanda M (2015) Small-scale spatial variability of turbulence statistics, (co)spectra and turbulent kinetic energy measured over a regular array of cube roughness. Environmental Fluid Mechanics 15(2):329–348
Scarano F, Riethmuller ML (2000) Advances in iterative multigrid piv image processing. Experiments in Fluids 29(1):S051–S060
Smagorinsky J (1963) General circulation experiments with the primitive equations: I. the basic experiment. Monthly weather review 91(3):99–164
Tomas J, Eisma H, Pourquie M, Elsinga G, Jonker H, Westerweel J (2017) Pollutant dispersion in boundary layers exposed to rural-to-urban transitions: varying the spanwise length scale of the roughness. Boundary-Layer Meteorology 163(2):225–251
Tomas JM, Pourquie MJBM, Jonker HJJ (2016) Stable stratification effects on flow and pollutant dispersion in boundary layers entering a generic urban environment. Boundary-Layer Meteorology 159(2):221–239
Xie Z, Castro IP (2006) LES and RANS for turbulent flow over arrays of wall-mounted obstacles. Flow, Turbulence and Combustion 76(3):291–312
Xie ZT, Coceal O, Castro IP (2008) Large-Eddy Simulation of Flows over Random Urban-like Obstacles. Boundary-Layer Meteorology 129(1):1–23
Yakhot A, Liu H, Nikitin N (2006) Turbulent flow around a wall-mounted cube: A direct numerical simulation. International Journal of Heat and Fluid Flow 27(6):994–1009
Yue W, Meneveau C, Parlange MB, Zhu W, Kang HS, Katz J (2008) Turbulent kinetic energy budgets in a model canopy: comparisons between LES and wind-tunnel experiments. Environmental Fluid Mechanics 8(1):73–95
Zang Y, Street RL, Koseff JR (1993) A dynamic mixed subgridscale model and its application to turbulent recirculating flows. Physics of Fluids A: Fluid Dynamics 5(12):3186–3196